Monocular 3D Object Detection in Cylindrical Images from Fisheye Cameras

Elad Plaut, Erez Ben Yaacov, and Bat El Shlomo

General Motors, Advanced Technical Center, Israel
{elad.plaut, erez.benyaacov, batel.shlomo}@gm.com

Abstract. Detecting objects in 3D from a monocular camera has been successfully demonstrated using various methods based on convolutional neural networks. These methods have been demonstrated on rectilinear perspective images equivalent to being taken by a pinhole camera, whose geometry is explicitly or implicitly exploited. Such methods fail in images with alternative projections, such as those acquired by fisheye cameras, even when provided with a labeled training set of fisheye images and 3D bounding boxes. In this work, we show how to adapt existing 3D object detection methods to images from fisheye cameras, including in the case that no labeled fisheye data is available for training. We significantly outperform existing art on a benchmark of synthetic data, and we also experiment with an internal dataset of real fisheye images.

1 Introduction

1.1 3D Object Detection and the Pinhole Camera Model

Object detection in 3D is a crucial task in applications such as robotics and autonomous driving. State-of-the-art methods use convolutional neural networks (CNN) that rely on multiple sensors such as cameras, LiDAR and radar. Yet, methods based only on a monocular camera have shown promising results, and these are important in cases where only a monocular camera is available.

Previous works have explicitly or implicitly assumed the pinhole camera model and have been demonstrated on datasets of perspective images. In the pinhole camera model, a point in 3D space in camera coordinates $[X, Y, Z]$ is projected onto the 2D perspective image by multiplication with the camera intrinsic matrix:

$$Z \begin{bmatrix} u \\ v \\ 1 \end{bmatrix} = \begin{bmatrix} f_X & \gamma & u_0 \\ 0 & f_Y & v_0 \\ 0 & 0 & 1 \end{bmatrix} \begin{bmatrix} X \\ Y \\ Z \end{bmatrix}, \tag{1}$$

where f_X, f_Y are the focal lengths along the X, Y axes (often $f_X \approx f_Y$); γ is the skew coefficient, which is often 0; u_0, v_0 represent the principal point (ideally the center of the image); and u, v are the coordinates of the projected point on the image.
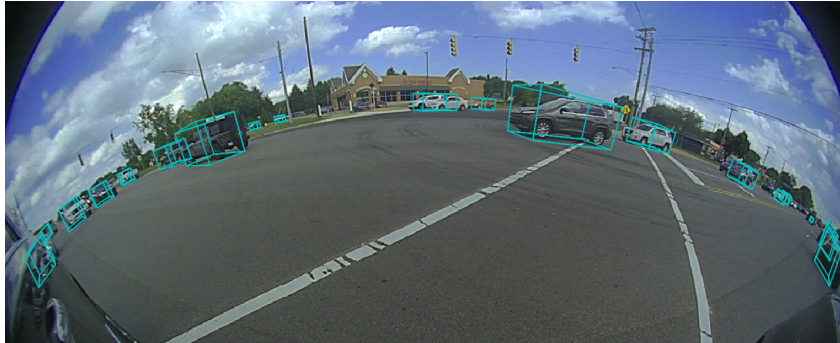
Fig. 1: 3D objects detected in a fisheye image using our method. No labeled fisheye images were used to train this model

From Eq. (1), it is clear that a 3D object with width ΔX and height ΔY has a magnification inversely proportional to Z. The size of the 2D box enclosing the projected object on the image is

$$\Delta u = \frac{f_X}{Z} \Delta X, \tag{2}$$

$$\Delta v = \frac{f_Y}{Z} \Delta Y. \tag{3}$$

This implies that perceived objects become smaller as they become more distant, where distance is measured along the Z axis. Objects with a constant Z may move along the X and Y axes, thereby significantly changing their Euclidean distance from the camera $\sqrt{X^2 + Y^2 + Z^2}$, while their projected size remains constant and their appearance remains similar. The dependence of the projected objects on Z provides cues that allow deep neural networks to predict the 3D location of objects from a monocular image. Some 3D object detection methods [1] [2] have explicitly added the dimensions of the predicted 2D bounding box as inputs to the object distance estimator.

A point in 3D with a viewing angle θ is projected onto the 2D perspective image at a distance r from the principal point such that

$$r = f \tan \theta. \tag{4}$$

This means that an object at a viewing angle approaching $90°$ is projected infinitely far from the principal point on the image plane, regardless of its 3D Euclidean distance from the camera. Objects at viewing angles larger than $90°$ cannot be represented at all. For this reason, the perspective projection is only used in cameras with a limited field-of-view (FoV).

1.2   Fisheye cameras

Wide FoV cameras are an important part of the sensor suite in areas such as robotics, autonomous vehicles and unmanned aerial vehicles (UAV). Such images

(a) Raw fisheye   (b) Perspective projection

(c) Cylindrical projection   (d) Spherical projection
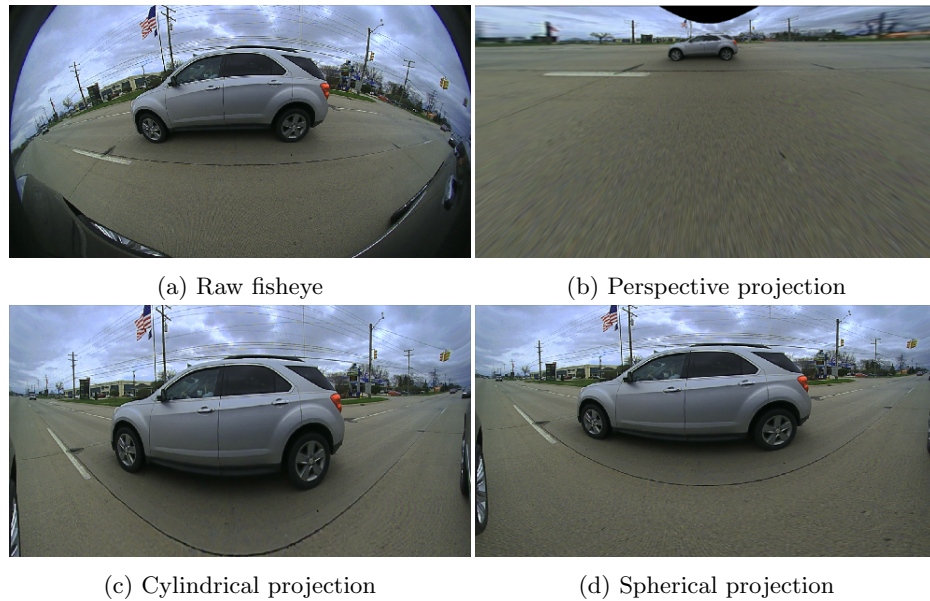
Fig. 2: Image projections

cannot be captured by a perspective camera. Instead, the images are represented in alternative projections, often the equidistant fisheye projection. A point in 3D with a viewing angle θ is projected onto the 2D fisheye image at a distance r from the principal point such that

$$r = f\theta. \tag{5}$$

Clearly, such images are able to capture objects at viewing angles of $90°$ and beyond. In the same manner that narrow FoV cameras may deviate from the pinhole camera model and require radial undistortion in order to obey Eq. (4), fisheye cameras may also deviate from the equidistant fisheye model and require radial undistortion in order to obey Eq. (5).

Fisheye images (Fig. 2a) appear very different from perspective images, and object detection models trained on perspective images do not always generalize well to fisheye images even in 2D. In 3D, objects at the same distance are not invariant as they are in perspective images - they become small, rotated and deformed as they move along the X and Y axes away from the image center. Such a geometry is not immediately compatible with convolutional neural networks, which are translation invariant by nature.

A naive approach is to attempt to undistort the fisheye image by warping it to a perspective image, potentially allowing the application of existing monocular 3D object detection methods and pretrained models. While this may be applicable to an image with a small FoV, when the FoV becomes large, the equivalent perspective image becomes impractical (Fig. 2b). Pixels in the fisheye
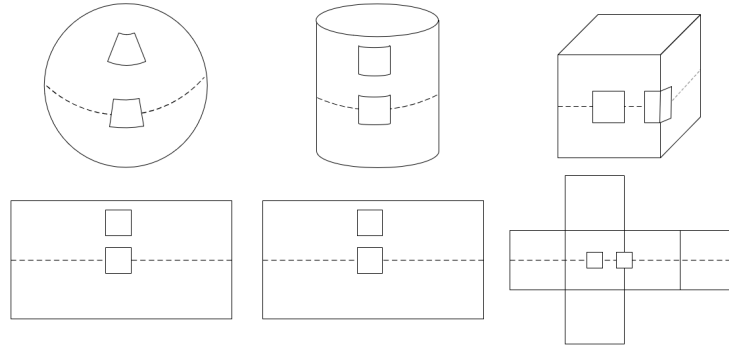
Fig. 3: Spherical, cylindrical and cubic projection surfaces and unfolded images

image that come from viewing angles approaching 90° are mapped to infinitely large distances in the perspective image, and pixels representing angles of more than 90° (i.e., behind the camera) have nowhere to be mapped. Furthermore, even for a smaller FoV, the periphery of the warped image is interpolated from much sparser pixels than the image center, and the wide range of magnifications creates an unfavorable trade-off between the FoV and the resolution required for the detection of objects at all possible viewing angles.

One solution is to break the fisheye image into several pieces and map each piece to a perspective image that simulates a different viewing direction. Fig. 3 (right) depicts projection onto a cube, where six pieces are stitched together to create a single piecewise linear (a.k.a. cube map) projection. While this enables the projection of 3D points from any viewing angle, it does not address the other problems mentioned above, and in addition it may complicate and degrade the detection of objects that occupy more than one of the image pieces.

1.3   Spherical and cylindrical panoramas

The spherical (equirectangular) projection is created by projecting the 3D scene onto a sphere as depicted in Fig. 3 (left), and it is useful when representing images from omnidirectional cameras or stitched panoramas. Fisheye images with any FoV may be warped to the spherical projection. In spherical images, an object at constant Euclidean distance is projected to different shapes depending on its location and becomes severely deformed as it moves away from the horizon (see Fig. 2 in [3]). Consequently, even 2D detection in spherical images is challenging.

Fisheye images may also be warped to the cylindrical projection, which is created by projecting the 3D scene onto a cylinder as illustrated in Fig. 3 (center). Compared to fisheye and spherical images, objects in cylindrical images appear much more similar to those in perspective images. Objects at a constant radial distance in cylindrical coordinates are projected to a constant shape as they move along the vertical and azimuth axes; straight vertical lines anywhere in 3D are projected to straight vertical lines on the image; and the horizon is projected

to a straight horizontal line across the center of the image (though all other horizontal lines become curved). In fact, a cylindrical image may be created by a perspective camera that rotates along an axis and captures a column of pixels at a time. Yet, unlike perspective images, cylindrical images can represent any FoV (excluding the points at 90° directly above or below the camera, but these are not required for common applications such as driving).

1.4   Contribution

Our main contributions are:

- We identify a unique analogy between the perception of distance in perspective images and in cylindrical images, which we use to develop a pipeline for 3D object detection in fisheye images.
- We propose a method for training models on datasets of perspective images or using models pretrained on such datasets, and then using them for 3D object detection in cylindrical images by applying a simple geometric transformation to the output.
- We propose optional steps for training, fine-tuning or self-supervised learning on the target domain, depending on the availability of training data.

2   Related work

Mono3D [4] parametrized the 3D bounding box of an object as (x, y, z, θ, c, t), where (x, y, z) is the center of the box, θ is the yaw, and c, t define the shape of the box. They train a neural network to predict these parameters in addition to the 2D bounding box. The method also leverages semantic segmentation, instance level segmentation and flat ground priors.

Deep3DBox [5] proposed to train a neural network to predict the 2D bounding box, the 3D bounding box dimensions and the observation angle. Then, it finds the center of the 3D box by minimizing the distance between its (2D-box enclosed) perspective projection and the predicted 2D box. Estimating the observation angle rather than the absolute yaw is preferred because objects with the same observation angle have a similar appearance in the image, but their yaw depends on the horizontal location within the image. As CNNs are generally shift-invariant, it is unreasonable to expect them to predict the absolute yaw (unless ad-hoc information that breaks translation invariance is added [6]).

By the same reasoning, when estimating depth from a single perspective image, it is more reasonable to train a CNN to predict Z rather than the Euclidean distance. ROI-10D [7] estimates the 3D bounding box using 10 network outputs: the RoI-relative 2D centroid, distance along the Z axis, 3D box dimensions, and a quaternion representing the rotation. The network is trained to minimize the error in the location of the 8 corners of the 3D box, built using the inverse perspective projection. The same parametrization was used in [2]. A simpler approach was proposed in [8], where the network is trained to predict the 2D

bounding box, the 3D dimensions, the observation angle and the distance Z. The 3D location of the object can be found by the inverse perspective projection, using Z together with the 2D point, taken either as the center of the 2D box or as a separately predicted keypoint.

Several methods [7], [9], [10], [11] use dense depth estimators to aid the prediction of object distances in addition to annotated 3D bounding boxes. Monocular depth estimators may be trained by supervised learning (e.g. from LiDAR) [12] or self-supervised learning (e.g. from stereo cameras or video) [13], [14], [15], [16], [17]. These methods too are designed for perspective images and define depth as the distance along the Z axis.

Several works have shown some success in 2D object detection in raw fisheye images [18], [19], [20], but none have been extended to monocular 3D detection. Methods for monocular dense depth estimation have been proposed for fisheye images [21], [22], [23] but have not been used in the context of object detection.

Methods for monocular dense depth estimation have been proposed for both spherical images [24], [25], [26], [27] and cylindrical images [28], yet research on 3D object detection has mostly been limited to perspective images. Object detection in cylindrical images has been successfully demonstrated only in 2D [29], [30], and models pretrained on perspective images generally perform decently on cylindrical images in 2D. Several works have shown success in 2D object detection in spherical images [3], [31] [32], [33], [34], but these methods rely on non-standard convolutions which do not run efficiently on hardware [35], and they have not been extended to 3D detection either.

One recent work [36] has proposed a method for 3D object detection in spherical panoramas. This work is perhaps the most closely related to ours. The authors regress the inverse Euclidean distance to the object and use the same network for perspective images and spherical images, the only difference being in the way they recover the 3D unit vector pointing towards the object. They train on synthesized spherical images by warping perspective images from the KITTI dataset [37] into spherical projections and transferring their style to that of the target domain. They evaluate on synthetic simulated data and qualitatively on unlabeled panoramic images. Their quantitative results show that applying both style transfer and spherical warping to the training images is actually worse than style transfer alone. Although they chose to use spherical projections, they cropped the images to a small vertical FoV around the horizon, where the projection surface is approximately cylindrical and the distortions depicted in Fig. 3 (left) are negligible.

3   Method

We detail our method as follows: in section 3.1 we describe training a model on perspective images; in section 3.2 we lay the basis for adapting the model to cylindrical images using geometric reasoning; section 3.3 describes the inference process for fisheye images. Sections 3.4 and 3.5 are optional steps for training on fisheye images in the target domain, depending on the availability of data.

3.1 Training on perspective images

The first step of our method is to train a monocular 3D object detection model on perspective images or to use a pretrained model. Any model that predicts Z as one of its outputs is suitable. The model may be trained on existing datasets of perspective images without any modifications.

We choose to implement a simple model. Similarly to [8], we train a network to predict the 2D bounding box, the 3D dimensions, the observation angle and the distance Z. Our 2D object detector is a flavor of Faster R-CNN [38], with a backbone that is ResNet50-like containing dilated convolutions. The entire network, including the 3D heads, is fully convolutional and trained end-to-end. For inference from perspective images, the 3D location of the object is found by the inverse perspective projection, using Z together with the 2D box center.

We do not use a special architecture for incorporating a dense depth estimator into the network; instead we simply apply a loss between the ground truth depth (defined as Z) and one of the feature channels near the network output. We do not explicitly use the predicted 2D bounding box dimensions as inputs to the object distance estimator, but they may be used; both the height and the width may be used, unlike methods designed for spherical projections in which only the height invariantly correlates with the distance.

3.2 Distance in cylindrical images

It is no coincidence that state-of-the-art monocular 3D object detection methods for perspective images are trained to predict distance as Z. CNNs seem to be able to pick up cues in the perspective image that correlate with Z. In fisheye, spherical and cubic images, there are no shift-invariant cues that correlate with Z or any other form of distance. In cylindrical images, however, there are.

Returning to Fig. 3, notice that the cylindrical projection is distinctive in that a square with constant area in the image is corresponds to a shape on the surface that is shift-invariant. A point in 3D space in camera coordinates $[X, Y, Z]$ is projected onto the cylindrical image by the following transformation:

$$\begin{bmatrix} u \\ v \\ 1 \end{bmatrix} = \begin{bmatrix} f_\phi & 0 & u_0 \\ 0 & f_y & v_0 \\ 0 & 0 & 1 \end{bmatrix} \begin{bmatrix} \phi \\ y \\ 1 \end{bmatrix}, \tag{6}$$

where

$$\begin{bmatrix} \phi \\ y \\ \rho \end{bmatrix} = \begin{bmatrix} \text{atan2}(X, Z) \\ Y/\sqrt{X^2 + Z^2} \\ \sqrt{X^2 + Z^2} \end{bmatrix}, \qquad \begin{bmatrix} X \\ Y \\ Z \end{bmatrix} = \rho \begin{bmatrix} \sin(\phi) \\ y \\ \cos(\phi) \end{bmatrix} \tag{7}$$

are the transformations between Cartesian and cylindrical coordinates; $f_\phi = \frac{W}{\Delta\phi}$, where W is the desired width of the cylindrical image and $\Delta\phi$ is the horizontal FoV; $f_y = \frac{H}{2\sin(\Delta\lambda/2)}$, where H is the desired height of the cylindrical image and $\Delta\lambda$ is the vertical FoV; we assumed the skew coefficient is zero; u_0, v_0 represent

the principal point (and may be assigned the values $\frac{W}{2}$ and $\frac{H}{2}$ respectively); and u, v are the coordinates of the projected point on the image.

From this equation, it is clear that an object with angular width $\Delta\phi$ and height Δy is projected onto the cylindrical image as a box whose width is $f_\phi \Delta\phi$ and height is $f_y \Delta y$. Unless the object is very large or in very close proximity to the camera, $\Delta X \approx \rho\Delta\phi$. Thus, a 3D object with width ΔX and height ΔY is projected onto the cylindrical image as a 2D box whose dimensions are

$$\Delta u = f_\phi \Delta\phi \approx \frac{f_\phi}{\rho}\Delta X, \tag{8}$$

$$\Delta v = f_y \Delta y = \frac{f_y}{\rho}\Delta Y. \tag{9}$$

This implies that projected objects become smaller as they become more distant, where distance is measured along the cylindrical ρ axis. Objects with a constant ρ may move along the ϕ and y axes, while their projected size remains constant and their appearance remains similar. The dependence of the projected objects on ρ in cylindrical images is identical to the dependence of projected objects on Z in perspective images (compare to Eq. (2), (3)).

To complete the equivalence, the width and height of the cylindrical image should be chosen such that $\frac{f_\phi}{f_y} = \frac{f_X}{f_Y}$, which occurs for an aspect ratio of

$$\frac{W}{H} = \frac{f_X \Delta\phi}{2f_Y \sin\left(\frac{\Delta\lambda}{2}\right)}. \tag{10}$$

3.3   Inference - fisheye images

Fisheye images are first warped to cylindrical projections with the aspect ratio from Eq. (10). The warping remaps pixels using predefined mappings and its computation time is typically negligible compared to the model inference time. The inverse mapping is created by using the inverse cylindrical intrinsic matrix to compute a 3D vector for each pixel in the cylindrical image, and then projecting it onto the fisheye image using the fisheye camera calibration.

The cylindrical image is used as input to the monocular 3D object detector that was trained on perspective images. The model is unfamiliar with the cylindrical projection and processes the input as if it were a perspective image. Let us examine the properties of the equivalent scene that would create the image if it were a perspective projection. Recall, the outputs of the model are the 2D bounding box, the 3D dimensions, the observation angle and the distance Z.

Objects in cylindrical images appear only slightly deformed compared to perspective images, and 2D detection accuracy should be high. The obvious difference between perspective images and cylindrical images is in the way a 3D vector pointing towards the object is computed from the 2D bounding box center $[u, v]$. In perspective images, Eq. (1) is used to solve for this vector in Cartesian coordinates. In cylindrical images, Eq. (6) is used to solve for this vector in cylindrical coordinates $[\phi, y, \rho]$, and its Cartesian coordinates may be recovered

using Eq. (7). This is a trivial modification to the output interpretation that is required by the projection geometry, and it has been used in previous works (including the spherical projection in [36]).

The 3D dimensions of an object and its observation angle are inferred from its appearance, which in the cylindrical projection is similar to its appearance in perspective images. This excludes objects that are very large or in very close proximity to the camera. Thus, with the exception of such objects, the model outputs for 3D dimensions and observation angle may be used without any modification. The yaw is found as usual using the observation angle and ϕ.

Finally, we exploit the analogy between Eq. (2), (3) and Eq. (8), (9). An object at cylindrical radial distance ρ is projected onto the cylindrical image similar to the manner that an object with a forward distance Z is projected onto a perspective image. Therefore the distance output of a model which was trained to predict Z in perspective images must be interpreted as ρ in cylindrical images. As usual, in order to account for the change in focal length, the distance output must be scaled by the ratio of target and source focal lengths $\frac{f_\phi}{f_X} = \frac{f_y}{f_Y}$.

3.4 Self-supervised learning for domain adaptation

The geometry of the projection may not be the only difference between the perspective training images and the target domain of cylindrical images. There may also be a difference in the styles of the datasets. Often, fisheye images from the target domain are available, but they are not annotated with 3D bounding boxes. Unlabeled data may be used for self-supervised learning as an additional loss to be trained jointly in multitask learning to aid domain transfer [39]. This is simpler than using a neural network to transfer the style of the training images to that of the target domain. As our self-supervised task we choose rotation prediction [40].

Sometimes, LiDAR point cloud data is available during training time together with fisheye images in large quantity while annotated 3D bounding boxes are not. The LiDAR points can be projected onto the cylindrical image, creating a depth map where depth is defined as ρ. This depth map may be used to train a monocular dense depth estimator in the target domain, and unlike other self-supervised tasks such as rotation prediction it contains 3D information. If LiDAR data is not available, a monocular dense depth estimator may still be trained in the target domain using unsupervised methods based on ego-motion [28]. In the source domain, our model was trained on perspective images using an auxiliary loss between the LiDAR ground truth depth (defined as Z) and one of the feature channels near the network output. In the case that fisheye images with LiDAR are available, the same feature channel may be jointly trained to predict a depth map of ρ for those images (warped to cylindrical projections).

### 3.5 Training or fine tuning on labeled fisheye images

The analogy between the geometry of perspective images and cylindrical images is only approximate, and it is especially inaccurate for objects that are very large
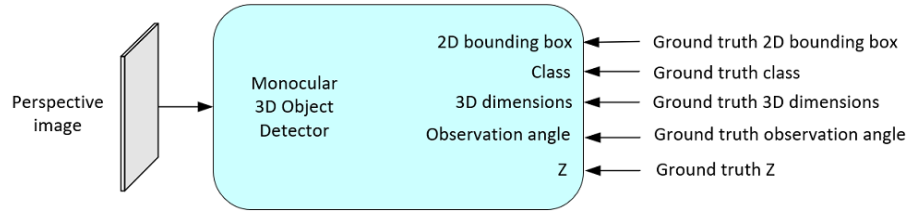
(a) Training a monocular 3D object detection model on perspective images using Z as the ground truth distance. No special network architecture or training procedure is required
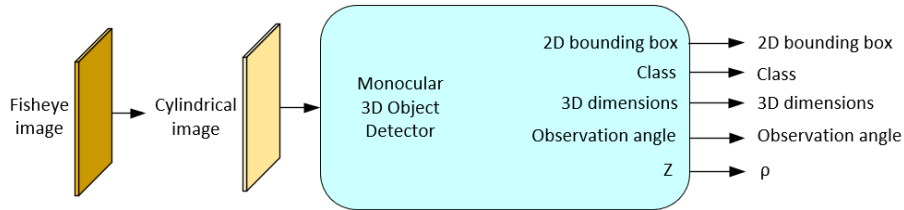
(b) Using the same model to detect objects in fisheye images by warping them to cylindrical images and interpreting the distance output as the cylindrical ρ
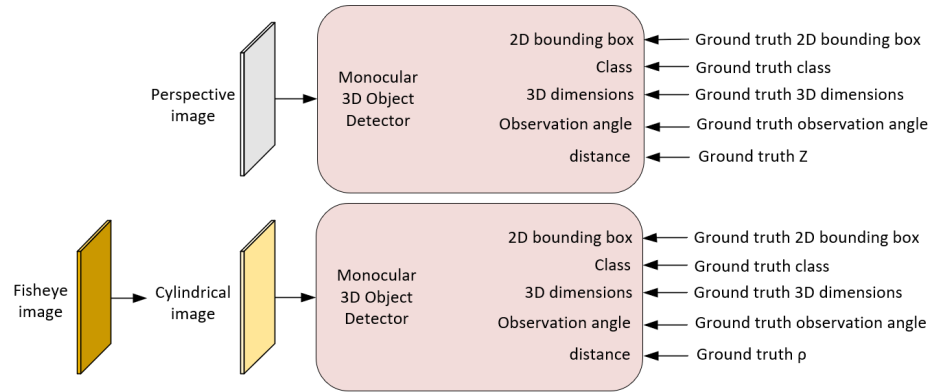
(c) Training a model jointly on both perspective and cylindrical images

Fig. 4: Training and inference configurations

(e.g. trucks, buses) or in very close proximity to the camera. The approximation $\Delta X \approx \rho \Delta \phi$ does not hold for such objects, therefore interpreting the Z output of the perspective model as ρ for cylindrical images is inaccurate.

Moreover, such objects do not have a discernible observation angle when viewed in the cylindrical projection. A large object that has a cuboid shape in 3D is projected onto the cylindrical image in the same way that a banana-shaped object is projected onto a perspective image. This can be seen in Fig. 2c, where

Table 1: Results for the synthetic panorama dataset

Model	2D-AP	3D-mAP	AOS	IoU	Dist. Err.
Our method	**0.472**	**0.301**	**0.419**	**0.360**	**0.883**
[36]	0.447	0.203	0.157	0.265	1.143

the front of the vehicle appears to be facing slightly away from the camera but the back of the vehicle appears to be facing slightly towards the camera. The equivalent scene that would create the image if it were a perspective projection contains deformed vehicles. These activate features that the observation angle prediction relies on which are out of distribution. As a result, a monocular 3D object detector that was trained on perspective images would not be able to accurately estimate the observation angle for such objects.

If labeled fisheye data is available, even in small quantity, it may be used to fine-tune the model to more accurately detect 3D objects in cylindrical images. When training on perspective images, the network is trained to predict Z. When training on cylindrical images, the same network output is trained to predict ρ. All other labels remain unmodified. Such models are no longer limited to objects that are not too large and not too near. Fig. 4 illustrates the different modes of operation of our method.

4   Experiments

4.1   Synthetic panoramic data

We evaluated our results on the synthetic panorama dataset from [36].[1] We trained our 3D object detector on the KITTI 3D Object training set [37]. We applied simple augmentations (mirroring, color, brightness and random cropping), but no style transfer or projection warping. In addition to the losses related to the 3D bounding boxes, we applied an ℓ_1 loss between the Z values of projected Velodyne LiDAR points and one of the feature channels near the network output. For domain adaptation, we predicted the rotation of square crops from the target domain as an auxiliary task. We used the method from [41] to dynamically adjust the weights of all the different tasks during training.

At inference, we warped the spherical panoramas to cylindrical projections and used our model, trained on perspective KITTI images, to detect 3D objects by interpreting the distance output as the cylindrical ρ.

Our method outperforms the best model from [36] in both 2D and 3D metrics: 2D-AP (defined using IoU $>$ 0.5 between 2D bounding boxes), 3D-mAP (as

---

[1] We report results for v2 of their dataset, which includes labels that were missing in the dataset version used in their original paper. We also include 3D detection metrics that were not reported in their original paper which they added to their evaluation later. For more information please visit their website which is linked in their paper.

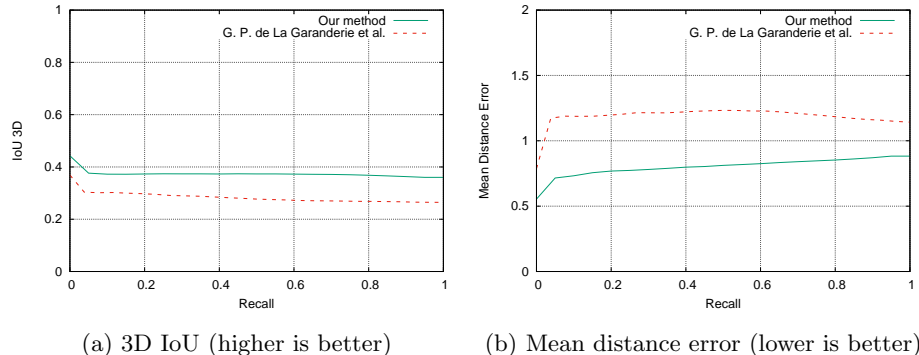(a) 3D IoU (higher is better)   (b) Mean distance error (lower is better)

Fig. 5: Synthetic panorama dataset results of our method and [36]

defined in [42]), average orientation similarity (AOS), mean 3D volumetric IoU and mean Euclidean distance error. Table 1 summarizes these results. Fig. 5a shows the 3D IoU of our model compared to the best model from [36], and Fig. 5b compares the mean distance errors for various detection thresholds.

4.2   Real fisheye data

We tested our method on data from real fisheye cameras. We collected a set of 3,172 test images of roads using a fisheye camera with a horizontal FoV of 190° and a vertical FoV of 107°. We warped them to the cylindrical projection with image size 620×1280 and annotated 3D bounding boxes for the vehicles in the images. We collected a separate set of 5,908 fisheye images which we left unlabeled for self-supervised learning, and we also collected LiDAR data.

We trained a model on the nuScenes dataset [42] similar to the one trained on KITTI in the previous experiment. In addition to rotation prediction, we used LiDAR points projected onto the cylindrical images to apply a dense depth estimation loss in the target domain. Finally, we annotated only 58 out of the 5,908 fisheye training images and fine-tuned the model using this very small number of labeled samples (we trained only a small number of parameters near the outputs while the rest of the network weights remained fixed).

The results of an ablation study are summarized in Table 2. Using LiDAR data for self-supervised learning in the target domain improved the distance error compared to using rotation only. Fine-tuning on the tiny labeled fisheye dataset improved both the observation angle similarity and the distance error.

Fig. 1 and Fig. 7 show examples of objects detected by the model from the first row in Table 2, projected onto the fisheye images. Detection is accurate even for the vehicles that are distant and standing on elevated ground. Fig. 6 shows an example of a typical failure case of that model (an adjacent vehicle in the neighboring lane), and the successful prediction after fine-tuning on the tiny labeled fisheye dataset. For the sake of clarity, all detections other than the discussed vehicle were removed from Fig. 6.

Table 2: Results for real fisheye data

Source domain (nuScenes)			Target domain (fisheye)			Results	
Rotation	LiDAR	Labels	Rotation	LiDAR	Labels	AOS	Distance Err.
✓	✓	✓	✓	✗	✗	0.989	1.61 m
✓	✓	✓	✓	✓	✗	0.984	1.22 m
✓	✓	✓	✓	✗	✓	0.991	0.74 m
✓	✓	✓	✓	✓	✓	**0.994**	**0.65 m**

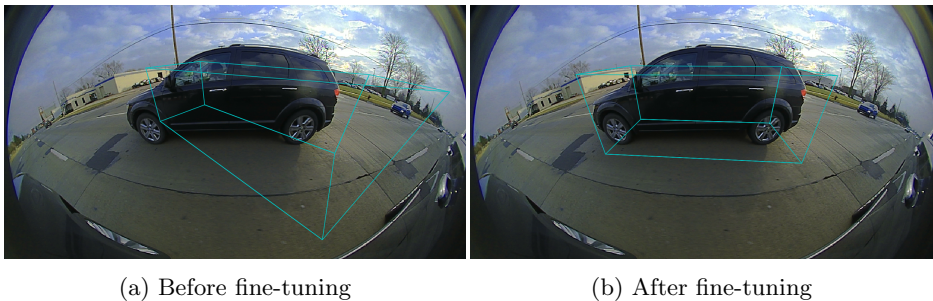
(a) Before fine-tuning   (b) After fine-tuning

Fig. 6: (a) A typical failure case of the model trained on perspective images, and (b) successful prediction after fine-tuning on a tiny labeled fisheye dataset

5 Conclusions

In this work, we have outlined a method for adapting monocular 3D object detectors to the fisheye domain based on a unique analogy between object distance perception in perspective images and in cylindrical images. Using our method, one can leverage powerful existing network architectures and models pretrained on massive labeled perspective image datasets and use them to detect objects in images from fisheye cameras. The same model may be used for perspective images and cylindrical images from fisheye cameras, the only difference being in the way the network output is interpreted.

We showed the limitations of using our method with no labeled fisheye training images, and that these may be overcome by fine-tuning on a tiny training set of labeled fisheye images. The scenario of large training sets of perspective images yet little or no labeled fisheye data is common in important computer vision tasks such as autonomous driving, and we hope that our method can help address such situations.

We do not require retraining models on fisheye data or the use of special augmentations, nor do we rely on a specific network architecture or non-standard convolutions. In contrast to the spherical projection, our method is independent of vertical shifts and may trivially be used to detect objects at large vertical viewing angles (e.g. lane markings and road edges, objects in indoor scenes, UAV imagery). We also do not rely on flat ground priors or make any assump-

tions about the 3D scene, and our method is applicable to objects that do not necessarily touch the ground (e.g. traffic lights).

We demonstrated our method for naive regression of the distance, but one could similarly adapt other monocular 3D object detection methods to cylindrical coordinates. We experimented with images from equidistant fisheye cameras and synthetic spherical panoramas, both of which were warped to cylindrical projections, but our method is not limited to these types of images. Other image projections used for representing large fields-of-view (e.g. the stereographic, orthographic and equisolid projections) may similarly be warped to the cylindrical projection and subsequently treated the same way.

Fig. 7: Results of our 3D object detection method for fisheye images

References

1. Haseeb, M.A., Guan, J., Ristić-Durrant, D., Gräser, A.: Disnet: A novel method for distance estimation from monocular camera. In: Workshop on Planning, Perception and Navigation for Intelligent Vehicles, International Conference on Intelligent Robots and Systems (IROS). (2018)
2. Simonelli, A., Bulò, S.R.R., Porzi, L., López-Antequera, M., Kontschieder, P.: Disentangling monocular 3d object detection. In: Proceedings of the IEEE International Conference on Computer Vision (ICCV). (2019)
3. Su, Y.C., Grauman, K.: Learning spherical convolution for fast features from 360 imagery. In: Advances in Neural Information Processing Systems (NIPS). (2017) 529–539
4. Chen, X., Kundu, K., Zhang, Z., Ma, H., Fidler, S., Urtasun, R.: Monocular 3d object detection for autonomous driving. In: Proceedings of the IEEE Conference on Computer Vision and Pattern Recognition (CVPR). (2016) 2147–2156
5. Mousavian, A., Anguelov, D., Flynn, J., Kosecka, J.: 3d bounding box estimation using deep learning and geometry. In: Proceedings of the IEEE Conference on Computer Vision and Pattern Recognition (CVPR). (2017) 7074–7082
6. Liu, R., Lehman, J., Molino, P., Such, F.P., Frank, E., Sergeev, A., Yosinski, J.: An intriguing failing of convolutional neural networks and the coordconv solution. In: Advances in Neural Information Processing Systems (NIPS). (2018) 9605–9616
7. Manhardt, F., Kehl, W., Gaidon, A.: Roi-10d: Monocular lifting of 2d detection to 6d pose and metric shape. In: Proceedings of the IEEE Conference on Computer Vision and Pattern Recognition (CVPR). (2019) 2069–2078
8. Zhu, J., Fang, Y.: Learning object-specific distance from a monocular image. In: Proceedings of the IEEE International Conference on Computer Vision (ICCV). (2019) 3839–3848
9. Xu, B., Chen, Z.: Multi-level fusion based 3d object detection from monocular images. In: Proceedings of the IEEE Conference on Computer Vision and Pattern Recognition (CVPR). (2018) 2345–2353
10. Weng, X., Kitani, K.: Monocular 3d object detection with pseudo-lidar point cloud. In: Proceedings of the IEEE International Conference on Computer Vision (ICCV) Workshops. (2019)
11. Wang, Y., Chao, W.L., Garg, D., Hariharan, B., Campbell, M., Weinberger, K.Q.: Pseudo-lidar from visual depth estimation: Bridging the gap in 3d object detection for autonomous driving. In: Proceedings of the IEEE Conference on Computer Vision and Pattern Recognition (CVPR). (2019) 8445–8453
12. Eigen, D., Puhrsch, C., Fergus, R.: Depth map prediction from a single image using a multi-scale deep network. In: Advances in Neural Information Processing Systems (NIPS). (2014) 2366–2374
13. Godard, C., Mac Aodha, O., Brostow, G.J.: Unsupervised monocular depth estimation with left-right consistency. In: Proceedings of the IEEE Conference on Computer Vision and Pattern Recognition (CVPR). (2017) 270–279
14. Pillai, S., Ambruş, R., Gaidon, A.: Superdepth: Self-supervised, super-resolved monocular depth estimation. In: 2019 International Conference on Robotics and Automation (ICRA), IEEE (2019) 9250–9256
15. Godard, C., Mac Aodha, O., Firman, M., Brostow, G.J.: Digging into self-supervised monocular depth estimation. In: Proceedings of the IEEE International Conference on Computer Vision (ICCV). (2019) 3828–3838

16. Zhou, T., Brown, M., Snavely, N., Lowe, D.G.: Unsupervised learning of depth and ego-motion from video. In: Proceedings of the IEEE Conference on Computer Vision and Pattern Recognition (CVPR). (2017) 1851–1858
17. Mahjourian, R., Wicke, M., Angelova, A.: Unsupervised learning of depth and ego-motion from monocular video using 3d geometric constraints. In: Proceedings of the IEEE Conference on Computer Vision and Pattern Recognition (CVPR). (2018) 5667–5675
18. Baek, I., Davies, A., Yan, G., Rajkumar, R.R.: Real-time detection, tracking, and classification of moving and stationary objects using multiple fisheye images. In: Intelligent Vehicles Symposium (IV), IEEE (2018) 447–452
19. Arsenali, B., Viswanath, P., Novosel, J.: Rotinvmtl: Rotation invariant multinet on fisheye images for autonomous driving applications. In: Proceedings of the IEEE International Conference on Computer Vision (ICCV) Workshops. (2019)
20. Goodarzi, P., Stellmacher, M., Paetzold, M., Hussein, A., Matthes, E.: Optimization of a cnn-based object detector for fisheye cameras. In: Proceedings of the IEEE International Conference of Vehicular Electronics and Safety (ICVES), IEEE (2019) 1–7
21. Kumar, V.R., Milz, S., Witt, C., Simon, M., Amende, K., Petzold, J., Yogamani, S., Pech, T.: Monocular fisheye camera depth estimation using sparse lidar supervision. In: International Conference on Intelligent Transportation Systems (ITSC), IEEE (2018) 2853–2858
22. Kumar, V.R., Milz, S., Witt, C., Simon, M., Amende, K., Petzold, J., Yogamani, S., Pech, T.: Near-field depth estimation using monocular fisheye camera: A semi-supervised learning approach using sparse lidar data. In: Proceedings of the IEEE Conference on Computer Vision and Pattern Recognition (CVPR) Workshops. (2018)
23. Kumar, V.R., Hiremath, S.A., Milz, S., Witt, C., Pinnard, C., Yogamani, S., Mader, P.: Fisheyedistancenet: Self-supervised scale-aware distance estimation using monocular fisheye camera for autonomous driving (2019)
24. Tateno, K., Navab, N., Tombari, F.: Distortion-aware convolutional filters for dense prediction in panoramic images. In: Proceedings of the European Conference on Computer Vision (ECCV). (2018) 707–722
25. Zioulis, N., Karakottas, A., Zarpalas, D., Daras, P.: Omnidepth: Dense depth estimation for indoors spherical panoramas. In: Proceedings of the European Conference on Computer Vision (ECCV). (2018) 448–465
26. Zioulis, N., Karakottas, A., Zarpalas, D., Alvarez, F., Daras, P.: Spherical view synthesis for self-supervised 360° depth estimation. In: International Conference on 3D Vision (3DV), IEEE (2019) 690–699
27. Won, C., Ryu, J., Lim, J.: Sweepnet: Wide-baseline omnidirectional depth estimation. In: International Conference on Robotics and Automation (ICRA), IEEE (2019)
28. Sharma, A., Ventura, J.: Unsupervised learning of depth and ego-motion from cylindrical panoramic video. In: Artificial Intelligence & Virtual Reality Conference (AIVR), IEEE (2019)
29. Bertozzi, M., Castangia, L., Cattani, S., Prioletti, A., Versari, P.: 360 detection and tracking algorithm of both pedestrian and vehicle using fisheye images. In: Intelligent Vehicles Symposium (IV), IEEE (2015) 132–137
30. Garnett, N., Silberstein, S., Oron, S., Fetaya, E., Verner, U., Ayash, A., Goldner, V., Cohen, R., Horn, K., Levi, D.: Real-time category-based and general obstacle detection for autonomous driving. In: Proceedings of the IEEE International Conference on Computer Vision (ICCV) Workshops. (2017)

31. Coors, B., Paul Condurache, A., Geiger, A.: Spherenet: Learning spherical repre-
    sentations for detection and classification in omnidirectional images. In: Proceed-
    ings of the European Conference on Computer Vision (ECCV). (2018) 518–533
32. Zhao, P., You, A., Zhang, Y., Liu, J., Bian, K., Tong, Y.: Reprojection r-cnn: A
    fast and accurate object detector for 360° images. arXiv preprint arXiv:1907.11830
    (2019)
33. Deng, F., Zhu, X., Ren, J.: Object detection on panoramic images based on deep
    learning. In: International Conference on Control, Automation and Robotics (IC-
    CAR), IEEE (2017) 375–380
34. Yu, D., Ji, S.: Grid based spherical cnn for object detection from panoramic images.
    Sensors **19**(11) (2019) 2622
35. Huang, Q., Wang, D., Gao, Y., Cai, Y., Dong, Z., Wu, B., Keutzer, K., Wawrzynek,
    J.: Algorithm-hardware co-design for deformable convolution. In: Conference on
    Neural Information Processing Systems (NeurIPS) Workshop. (2017)
36. Payen de La Garanderie, G., Atapour Abarghouei, A., Breckon, T.P.: Eliminating
    the blind spot: Adapting 3d object detection and monocular depth estimation to
    360 panoramic imagery. In: Proceedings of the European Conference on Computer
    Vision (ECCV). (2018) 789–807
37. Geiger, A., Lenz, P., Urtasun, R.: Are we ready for autonomous driving? the
    kitti vision benchmark suite. In: Conference on Computer Vision and Pattern
    Recognition (CVPR). (2012)
38. Ren, S., He, K., Girshick, R., Sun, J.: Faster r-cnn: Towards real-time object detec-
    tion with region proposal networks. In: Advances in neural information processing
    systems (NIPS). (2015) 91–99
39. Sun, Y., Tzeng, E., Darrell, T., Efros, A.A.: Unsupervised domain adaptation
    through self-supervision. arXiv preprint arXiv:1909.11825 (2019)
40. Gidaris, S., Singh, P., Komodakis, N.: Unsupervised representation learning by pre-
    dicting image rotations. In: International Conference on Learning Representations
    (ICLR). (2018)
41. Kendall, A., Gal, Y., Cipolla, R.: Multi-task learning using uncertainty to weigh
    losses for scene geometry and semantics. In: Proceedings of the IEEE Conference
    on Computer Vision and Pattern Recognition (CVPR). (2018) 7482–7491
42. Caesar, H., Bankiti, V., Lang, A.H., Vora, S., Liong, V.E., Xu, Q., Krishnan, A.,
    Pan, Y., Baldan, G., Beijbom, O.: nuscenes: A multimodal dataset for autonomous
    driving. arXiv preprint arXiv:1903.11027 (2019)